ACS APPLIED MATERIALS & INTERFACES

Research Article

www.acsami.org

Reduced Graphene Oxide–TaON Composite As a High-Performance Counter Electrode for $Co(bpy)_3^{3+/2+}$-Mediated Dye-Sensitized Solar Cells

Yan Li,[†] Hong Wang, Quanyou Feng, Gang Zhou, and Zhong-Sheng Wang*

Department of Chemistry, Lab of Advanced Materials, Collaborative Innovation Center of Chemistry for Energy Materials, Fudan University, 2205 Songhu Road, Shanghai 200438, P. R. China

Supporting Information

ABSTRACT: We report herein the investigation of TaON nanoparticles incorporating a reduced graphene oxide (RGO) nanocomposite as a counter electrode for application in $Co(bpy)_3^{3+/2+}$ (bpy = 2,2′-bipyridine)-mediated dye-sensitized solar cells (DSSCs). The RGO–TaON nanocomposite has been prepared by mixing graphene oxide (GO) and presynthesized TaON nanoparticles in ethanol/water followed by the facile hydrazine hydrate reduction of GO to RGO. Compared with RGO or TaON alone, the RGO–TaON nanocomposite shows a much higher electrocatalytic activity for the reduction of $Co(bpy)_3^{3+}$ species owing to synergistic effects, resulting in significantly improved solar-cell performance when it is applied as the counter electrode in DSSCs. An efficiency of 7.65% for the DSSC with the RGO–TaON counter electrode is obtained, competing with the efficiency produced by the Pt counter electrode; additionally, the former exhibits a much better electrochemical stability than the latter in a $Co(bpy)_3^{3+/2+}$ acetonitrile solution.

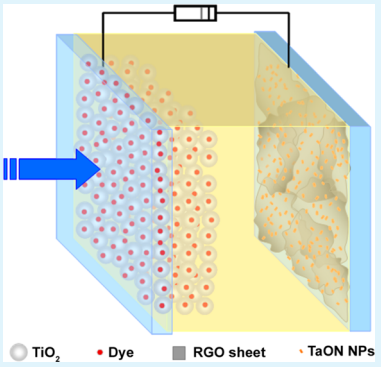

KEYWORDS: *reduced graphene oxide–TaON nanocomposite, $Co(bpy)_3^{3+/2+}$ redox couple, counter electrode, dye-sensitized solar cell*

1. INTRODUCTION

Ever since the pioneering work of O'Regan and Grätzel in 1991,[1] dye-sensitized solar cells (DSSCs) have continuously attracted great interest and currently represent the cutting edge of photovoltaic technologies owing to their high light-to-electricity conversion efficiency and cost-effective fabrication. A conventional DSSC consists of a dye-sensitized mesoporous nanocrystalline TiO_2 photoanode, an iodide/triiodide (I^-/I_3^-) redox couple-based electrolyte, and a platinized conductive glass as the counter electrode (CE). To improve the efficiency and long-term stability of DSSCs, great efforts have been focused on the research of new dye sensitizers,[2−5] electrolytes,[6−8] and photoanodes[9−12] as well as fundamental understanding.[13−15] More recently, polypyridine complexes of Co(II)/Co(III) coupled with donor (D)-π-bridge-acceptor (A) structured organic dyes has turned out to be one of the most promising routes to boost the efficiency of DSSCs, and a new record efficiency of 12.3% was achieved using the Co(II/III)tris(bipyridyl)-based redox electrolyte in conjunction with the D-π-bridge-A zinc porphyrin (YD2-*o*-C8) dye and organic Y123 dye, cosensitized TiO_2 anode, and Pt as the CE.[16]

As a crucial component, CE facilitates the electron translocation from the external circuit back to the electrolyte by catalyzing the reduction of the oxidized species of the redox couple to complete the electric circuit. Thus, CE materials with excellent electrocatalytic activity and high electrical conductivity are in demand. Although Pt is really outstanding, it is a limited resource, restricting the further development of DSSCs.[17,18] This has stimulated great efforts to develop alternative noble-metal-free materials capable of replacing Pt as electrocatalysts, such as inorganic compounds,[19,20] conducting polymers,[21−23] and carbon materials.[24−28] Graphene, a monolayer of carbon atoms packed into a dense honeycomb crystalline structure, has currently emerged as a fascinating material for CE studies in DSSC.[26,28−30] As the intermediate state between graphene oxide (GO) and graphene, reduced graphene oxide (RGO) possesses several types of oxygen-containing functional groups (−OH, =O, −COOH) and lattice surface defects that are believed to support electrocatalytic sites and interact with metal nanoparticles (NPs) or metal oxides and nitrides. For this reason, RGO is more favorable for CE materials than the perfect, fully reduced and defect-free graphene.

Owing to their Pt-like catalytic activity together with their high thermal conductivity,[18,31,32] transition-metal carbides, nitrides, and oxides have been extensively applied in the fields of methanol oxidation, gas sensors, and field emitters[33−35] but less so in DSSCs.[18,36−38] Herein, we report the application of TaON NP-embedded RGO nanocomposite (RGO–TaON) as the CE in D-π-A-structured organic dye (FNE29, Figure S1)-sensitized and $Co(bpy)_3^{3+/2+}$-mediated (Figure S2) DSSCs. The electrochemical analyses demonstrate that the RGO–TaON nanocomposite exhibits comparable catalytic activity for

Received: June 18, 2013
Accepted: July 15, 2013
Published: July 15, 2013

   dx.doi.org/10.1021/am402353m | ACS Appl. Mater. Interfaces 2013, 5, 8217−8224

the reduction of $Co(bpy)_3^{3+}$ species and superior electrochemical stability relative to that of Pt.

2. EXPERIMENTAL SECTION

2.1. Synthesis of TaON Nanoparticles. TaON NPs were prepared through an improved Ca-assisted urea route presented by Gao.[39] After 0.50 g of $TaCl_5$ powder, 0.14 g of $CaCO_3$, and 0.75 g of urea were successively dissolved in 2 mL of methanol, the solution was gradually dried to gel under stirring. After calcination in pure N_2 under 120 Pa at 780 °C for about 6 h, the resulting solid powder was treated with 1 M HCl for 1 day and washed repeatedly with deionized water to remove Ca species. The obtained TaON NPs were ultrasonically dispersed in ethanol.

2.2. Preparation of RGO and RGO−TaON Nanocomposites. GO was synthesized from natural graphite powder (Alading Reagent, Inc.) via the modified Hummers method.[40] The RGO suspension was directly prepared by hydrazine hydrate ($N_2H_4{\cdot}H_2O$, 10 wt %, Sinopharm Chemical Reagent Co., Ltd.) reduction of 0.25 mg mL^{-1} of exfoliated GO suspension in water, which was obtained by ultrasonication for 0.5 h according to the literature.[41] To prepare the GO−TaON nanocomposite, a certain amount of TaON/ethanol suspension (0.2 mg mL^{-1}) was added to 10 mL of GO solution under ultrasonic conditions, and a transparent mixture without any aggregates was obtained. After adding 25 μL of hydrazine hydrates and heating in an oil bath at 98 °C for about 5 h, GO was reduced to RGO, and the RGO−TaON nanocomposite suspension was obtained. TaON NPs deposited on RGO nanosheets with different RGO/TaON weight ratios of 1/0.5, 1/1, 1/1.5, 1/2, 1/2.5, and 1/3 were prepared to optimize the constitutional ratio. For comparison, a blend of RGO and TaON (denoted as RGT) was obtained by mixing RGO and TaON suspensions under ultrasonication.

2.3. Fabrication of CEs and DSSCs. The CEs of RGO, TaON, RGT, and RGO−TaON were prepared through a simple drop-casting method. A certain amount of RGO, TaON, RGT, or RGO-TaON suspension was drop casted onto the surface of a drilled FTO substrate (fluorine-doped SnO_2, 7 Ω sq^{-1}, Nippon Sheet Glass Co., Ltd.), which was masked by scotch tape (3M) with an aperture area of 0.6 × 0.6 cm^2 and dried at room temperature. The adhesion of these RGO-based films to FTO was firm enough to fabricate DSSCs. As a reference, a pyrolytic Pt CE was also prepared by the deposition of 20 μL of H_2PtCl_6 in ethanol (5 mM) on a 1.6 × 1.6 cm^2 FTO glass followed by 380 °C heat treatment for about 30 min.

Eight-micrometer-thick TiO_2 films were screen printed on FTO glass and sensitized with a D-π-A-structured metal-free organic dye (FNE29, Figure S1). The dye-sensitized TiO_2 photoanode and the CE were separated by a hot-melt Surlyn film (30 μm) and sealed through hot pressing. Next, the electrolyte of the $Co(bpy)_3^{3+/2+}$ redox couple (Figure S2) in acetonitrile was injected into the interspace between the anode and the CE. Finally, the holes on the back of the CE were sealed with Surlyn films covered by a thin glass slide under heat. The active area of the DSSCs was 0.2304 cm^2. Symmetric dummy cells with an active area of 0.36 cm^2 were assembled with two identical CEs filled with the electrolyte. The synthesis of FNE29 and the $Co(bpy)_3^{3+/2+}$ redox couple are detailed in the Supporting Information. Moreover, DSSCs with N719 (cis-di(isothiocyanato)-bis-(2,2′-bipyridyl-4,4′-dicarboxylato)ruthenium-(II) bis-tetrabutylammonium) sensitizer and I^-/I_3^- redox electrolyte (0.1 M LiI, 0.05 M I_2, 0.6 M 1,2-dimethyl-3-*n*-propylimidazolium iodide, and 0.5 M 4-*t*-butylpyridine in anhydrous acetonitrile) were also fabricated for comparison.

2.4. Characterization and Solar-Cell Performance Measurement. High-resolution transmission electron microscopy (HRTEM, JEM-2100F, JEOL) and field-emission scanning electron microscopy (FESEM, S-4800, Hitachi) were employed to study the morphologies of the materials. X-ray diffraction (XRD) patterns were performed with an X-ray powder diffractometer (D8 Advance, Bruker) with Cu Kα radiation (λ = 0.154 nm). Raman scattering measurements were performed at 25 °C with 633 nm excitation on a Renishaw spectrometer using a 100× objective. The Brunauer−Emmett−Teller (BET) specific surface area was analyzed by the BET equation using a surface-area analyzer (ASAP 2020, Micromeritics). Electrochemical impedance spectroscopy (EIS), cyclic voltammetry (CV), and Tafel polarization curves were performed on an electrochemical workstation (ZAHNER ZENNIUM CIMPS-1, Germany). The photocurrent density−voltage curves (J−V) of the DSSCs were recorded on a Keithley 2400 source meter under the illumination of AM1.5G simulated solar light coming from a solar simulator (Newport-94043A) equipped with a Xe lamp (450 W) and an AM1.5G filter. The light intensity was calibrated using a reference Si solar cell (Newport-91150) equipped with a KG-5 filter (Schott). A black mask with an aperture area of 0.2304 cm^2 was applied to the surface of the DSSCs (active area of 0.25 cm^2) to avoid stray light completely. Action spectra of the incident monochromatic photon-to-electron conversion efficiency (IPCE) for the solar cells were obtained with an Oriel-74125 system (Oriel Instruments). The intensity of monochromatic light was measured with a Si detector (Oriel-71640). Four parallel DSSCs for each sample were measured with a standard deviation error of less than 0.1% in absolute efficiency.

3. RESULTS AND DISCUSSION

3.1. Characterizations of TaON, RGO, and RGO−TaON Nanocomposites. X-ray diffraction (XRD) patterns of the as-prepared RGO−TaON nanocomposite, pure TaON, GO, and RGO are shown in Figure 1. The typical XRD pattern of GO

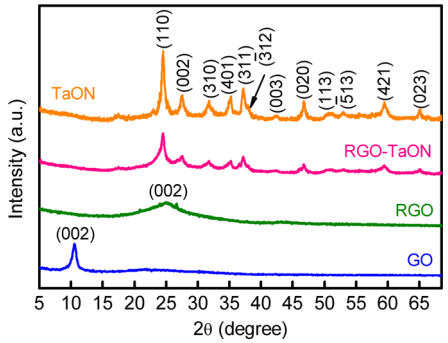

Figure 1. XRD patterns of the as-prepared TaON NPs, RGO, GO, and RGO−TaON.

with the AB stacking order[42] shows a strong and sharp (002) peak at 2θ = 10.5°. This peak is broadened and shifted to 2θ = 24.9° for RGO, which is attributed to the crystallographic plane of (002) in the graphitic structure[43] and suggests that the interlayer distance is reduced resulting from the removal of most of the oxygen-containing functional groups of GO.[29] All of the diffraction peaks for the as-prepared tantalum oxynitride products can be well indexed to γ-TaON (ICDD no. 01-076-3258), and these peaks are also clearly observed in the XRD pattern of the RGO−TaON nanocomposite. The absence of the peak at 10.5° for GO is ascribed to the fact that GO was reduced to RGO during the hydrothermal reaction. The XRD peak for RGO sheets was not resolved because of its low intensity and its peak overlap with the (110) peak for TaON. The adsorption of TaON NPs on exfoliated GO sheets prevented the aggregation and restacking of RGO sheets after reduction of GO, resulting in a low intensity for the (002) peak of RGO.[44,45]

The representative HRTEM and FESEM images of the as-prepared TaON, RGO, and RGO−TaON are displayed in Figure 2. The as-synthesized TaON are yellow NPs with a size of ∼22 nm (Figure 2a) and can be well dispersed in ethanol. The clear lattice fringes of 0.37 (110) and 0.64 nm (001) in the HRTEM image (Figure 2b) identifies γ-TaON and confirms its

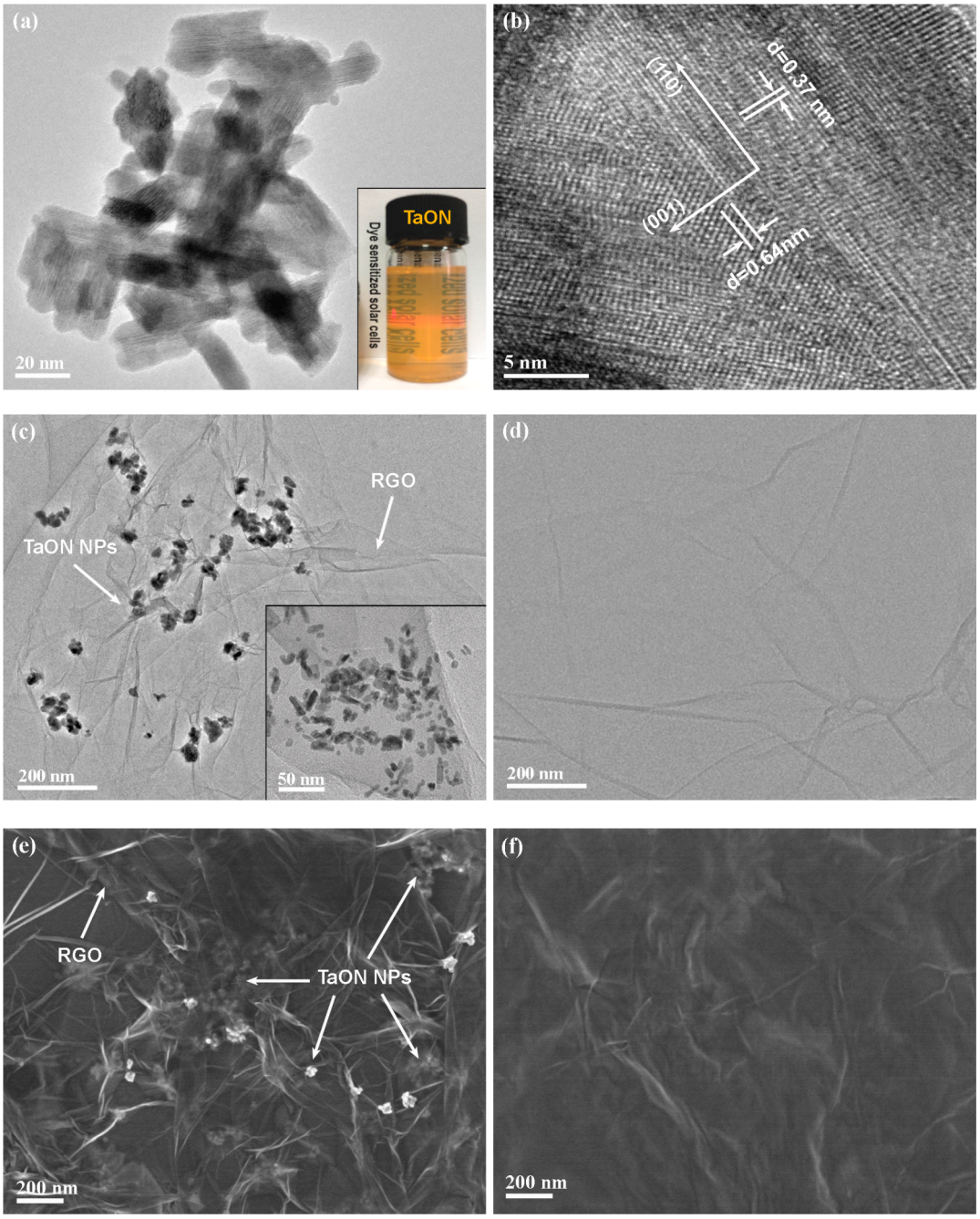

Figure 2. TEM (a) and HRTEM (b) images of the as-prepared TaON NPs, TEM images of the RGO-TaON nanocomposite (c) and RGO (d), and top-view FESEM images of the RGO−TaON (e) and RGO (f) CEs. The inset of panel a shows a photo of TaON NPs dispersed in ethanol. The inset of panel c shows the magnified image of RGO−TaON.

good crystallinity, which nicely fits with the results from the XRD analysis. This is also in agreement with the published work on TaON NPs.[39] Compared with bare RGO (Figure 2d), the TEM image of the RGO−TaON nanocomposite in Figure 2c reveals that the TaON NPs are embedded into the RGO layers or adsorbed on the surface of RGO. The particles inside can be observed through the transparent RGO sheets. A comparison of panels a and c in Figure 2 reveals that TaON NPs exhibit similar morphology and size. Figure 2e,f shows the top view of the drop-casted RGO−TaON and RGO films on FTO substrates, which serve as CEs in DSSCs. Obviously, the RGO CE has a relatively homogeneous and smooth morphology with nearly no shrinkage and folds, whereas the RGO−TaON composite is more corrugated with TaON NPs embedded in the RGO sheets.

The measured BET surface area of the TaON NPs, RGO, RGO−TaON, and RGT nanocomposites are 38.1, 12.3, 54.3, and 47.8 $m^2\ g^{-1}$, respectively. The specific surface area of the RGO−TaON composite is much higher than that of each component in the composite. By subtracting the contribution from the TaON NPs, the specific surface area of RGO in the RGO−TaON nanocomposite (weight ratio RGO/TaON = 1/1.5) is calculated to be 78.6 $m^2\ g^{-1}$, which is more than 6 times that of bare RGO. This indicates that more of the surface of RGO is available in the composite than in the close-packed bare RGO resulting from the pillaring effect of TaON NPs. As such,

dx.doi.org/10.1021/am402353m | ACS Appl. Mater. Interfaces 2013, 5, 8217−8224

RGO−TaON nanocompositse can be expected to be an effective electron-transport network to facilitate the reduction of Co(III) species at the catalyst/electrolyte interface. It is noted that the specific surface area of RGT is also higher than that of each component in the blend, suggesting that blending RGO with TaON can also promote an increase in the surface of RGO available.

Raman spectroscopy is the most sensitive and informative technique to characterize the disorder in sp^2 carbon materials. As shown in Figure 3, the D band is due to the breathing mode

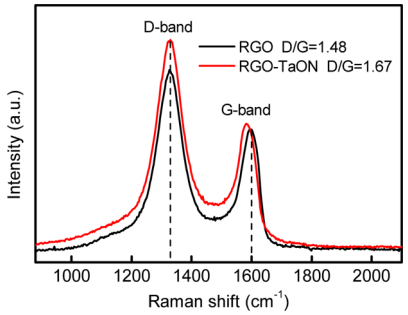

Figure 3. Raman spectra of RGO and the RGO−TaON nanocomposite.

of the aromatic rings (A_{1g}) and requires a defect for its activation, and the G band corresponds to optical E_{2g} phonons at the Brillouin zone center and is due to the bond-stretching motion of the sp^2 carbon pairs in both rings and chains. The intensity ratio of the D and G bands (D/G) is usually taken as an indication of the relative disorder present in graphitic structures.[42] In comparison with GO, both the D and G bands shift to a lower frequency (from 1332 to 1328 cm^{-1} for the D band and from 1602 to 1597 cm^{-1} for the G band, Figure S3), indicating the reduction of GO to RGO.[46] For the Raman spectrum of the RGO−TaON nanocomposite, the higher intensity ratio of D/G than that for RGO not only manifests the prevailing heterogeneous superstructure at the interface of RGO and TaON[47,48] but also indicates a higher density of the defects on the structure of the graphene, which is attributed to the formation of incoherent interfaces between TaON NPs and RGO nanosheets. In addition, the Raman peak of the G band shifts to a lower frequency from 1597 for RGO to 1583 cm^{-1} for the RGO−TaON nanocomposite. The shift indicates that the TaON NPs are chemically absorbed on the RGO sheets, which is attributed to the interaction of tantalum oxynitride with oxygen-containing groups on RGO. However, the Raman peak positions and the D/G ratio for RGT were not changed (Figure S4) when RGO and TaON were mixed directly. This indicates that mixing TaON NPs and GO first and then reducing GO to RGO is necessary to yield interactions between RGO and TaON. The main difference between the RGO−TaON composite and RGT is the interaction between RGO and TaON. The strong interactions between TaON and the hydroxyl groups on GO nanosheets cause the TaON NPs to be firmly loaded on GO sheets, ensuring that the TaON NPs are firmly adsorbed on the surface of RGO upon reduction of GO to RGO. The interactions between TaON and RGO can facilitate the electron transfer between TaON and RGO.

3.2. Electrochemical Properties of CEs. To investigate the electrocatalytic activity of the electrode materials as CEs for the reduction of $Co(bpy)_3^{3+}$ species in DSSCs, EIS spectra were recorded using symmetric cells (CE/electrolyte/CE) consisting of two identical CEs and a sandwiched thin layer of redox electrolyte solution (the same as the electrolyte used in DSSCs). For porous-structured electrode materials, three semicircles should be observed in the Nyquist plots:[49] a semicircle resulting from the Nernst diffusion impedance (Z_{pore}) in the electrode pores in the high-frequency region, a semicircle arising from the charge-transfer resistance (R_{ct}) and the corresponding constant-phase element (CPE) at the CE−electrolyte interface in the middle-frequency region, and a low-frequency semicircle corresponding to the Nernst diffusion impedance (Z_N) in the bulk electrolyte solution between the electrodes. However, Z_{pore} can be omitted in our case owing to the small amount of catalyst. As seen in Figure 4, only two semicircles show up in the EIS spectra (Nyquist plots) with or without bias potentials in the measured frequency range of 5×10^{-2} to 1×10^6 Hz, and the left arc shrinks whereas the right arc expands with the increase of the bias potentials. This indicates that the observed left arc should be attributed to the charge transfer at the CE−electrolyte interface, and the right arc should be attributed to the Nernst diffusion impedance in the bulk electrolyte.[49] Therefore, the Randles-type equivalent circuit diagram (inset of Figure 5) can be selected to fit the impedance spectra in which CPE describes the deviation from the ideal capacitance resulting from the roughness of the electrodes.

Electrocatalytic activities of the RGO−TaON nanocomposite with different weight ratios of 1/0.5, 1/1, 1/1.5, 1/2, 1/2.5, and 1/3 were investigated. As shown in Figure S5, the ratio of 1/1.5 produced the best electrocatalytic performance; thus, the

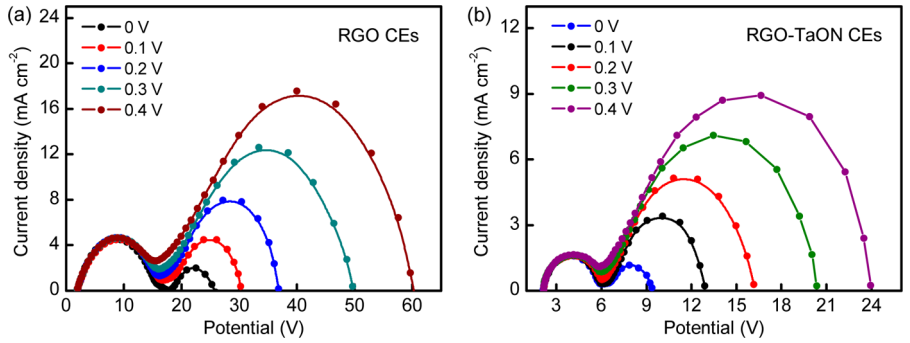

Figure 4. Nyquist plots of the electrochemical impedance spectra measured from 100 mHz to 100 kHz on symmetrical dummy cells with RGO (a) and RGO−TaON (b) CEs under bias potentials of 0, 0.1, 0.2, 0.3, and 0.4 V, respectively. The increase of Z_N with the bias potentials is the result of the depletion of Co ions from the bulk electrolyte.

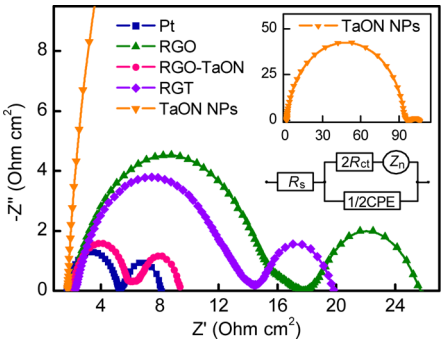

Figure 5. Nyquist plots of EIS for symmetric cells with two identical counter electrodes of RGO–TaON, RGO, RGT, TaON NPs, or Pt at different impedance ranges. The inset gives the equivalent circuit diagram. The cells were measured with the frequency range from 50 mHz to 100 kHz. R_s is the ohmic series resistance, R_{ct} is the charge-transfer resistance, Z_N is the bulk electrolyte diffusion impedance, and CPE is the constant-phase element. The bias potential is 0 V.

ratio of 1/1.5 was selected to conduct the following experiments. Figure 5 shows the Nyquist plots of EIS for CEs of RGO–TaON, RGT, RGO, TaON NPs, and Pt. The high-frequency intercept on the real axis represents theR_s. By fitting the impedance spectra using the Z-view software, the values of the impedance parameters are calculated using the total surface area of the catalysts on the electrode,[20] as summarized in Table 1. The total surface area obtained by the product of the specific BET surface area, loading amount, and the active apparent area (0.36 cm^2) of the electrode is 0.27, 0.11, 0.61, and 0.48 cm^2 for TaON, RGO, RGO–TaON, and Pt, respectively. Because catalytic performance depends on the total surface area of the material, it is more strict to compare the catalytic activity of the different materials normalized to the total surface area rather than the apparent area.[20]

As shown in Table 1, the R_s values show little difference between the four CEs, implying that the effect of various CEs caused by R_s on the photovoltaic performance is negligible. For the value of R_{ct}, the lower it is the higher the electrocatalytic performance of the CE on the reduction of $Co(bpy)_3^{3+}$ species. The R_{ct} for TaON, RGO, RGO–TaON, and Pt electrodes are 46.9, 6.9, 1.9, and 1.8 Ω cm^2, respectively. It is clear that TaON alone shows the largest R_{ct}, indicating it has the lowest catalytic ability among these CEs, and the R_{ct} of RGO is also much larger than that of Pt. Once TaON NPs are embedded in an RGO network, the R_{ct} value of the RGO–TaON nanocomposite is significantly reduced to 1.9 Ω cm^2, which is much smaller than that of each individual component and very close to that of Pt (1.8 Ω cm^2). This indicates RGO–TaON is a much better electrocatalyst than each individual component for the reduction of $Co(bpy)_3^{3+}$ species. Because the total surface area rather than the apparent area is used for the determination of R_{ct}, the enhanced electrocatalytic activity from each individual component to their nanocomposite should be attributed to the synergistic coupling effects between RGO and TaON.[50] The strong interaction between RGO and TaON in the RGO–TaON composite revealed by the D-band shift shown in the Raman spectra (Figure 3) promotes the charge transfer between them, which should be responsible for the observed synergistic effect.[50] In addition, ballistic conduction of charge carriers in 2D RGO ensures a better conductivity[51,52] for the RGO–TaON composite as compared to TaON (see Figure S6), which can also contribute to the improved electrocatalytic activity toward the reduction of $Co(bpy)_3^{3+}$ species. However, for the RGT sample obtained from the direct blending of RGO and TaON, R_{ct} is slightly reduced as compared to RGO; thus, the synergistic effect was not observed because of the absence of interactions between RGO and TaON in RGT (Figure S4). For this reason, the electrocatalytic activity of RGT seems to be the arithmetic summation of those for RGO and TaON. For the Nernst diffusion impedances of these CEs, compared with TaON (8.6 Ω cm^2) and RGO (7.4 Ω cm^2), RGO–TaON shows a much lower Z_N of 3.0 Ω cm^2, which is close to the value of Pt (2.7 Ω cm^2). This means the $Co(bpy)_3^{3+}$ species can be rapidly reduced to $Co(bpy)_3^{2+}$ under the catalysis of RGO–TaON so that diffusion of $Co(bpy)_3^{3+}$ seems to be accelerated.

Cyclic voltammetry (CV) curves of the same symmetrical cells used in EIS analysis with $Co(bpy)_3^{3+/2+}$ in acetonitrile as the electrolyte were further measured to compare the electrocatalytic activity of the four CE materials, as shown in Figure 6a. The plateau region of the CV curve exhibits the

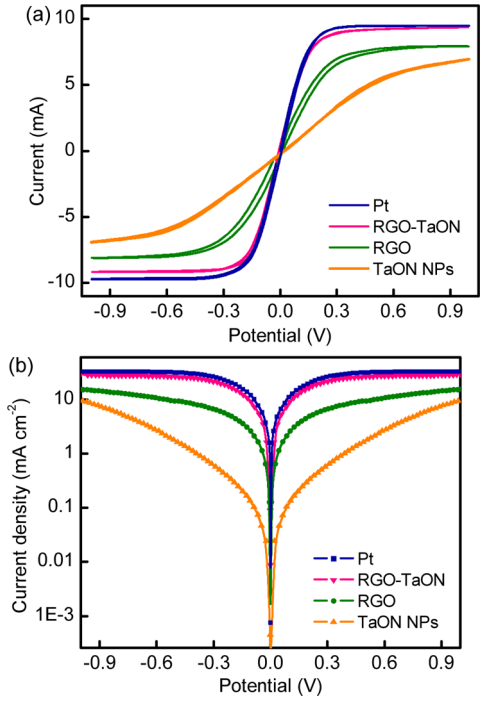

Figure 6. Cyclic voltammograms of dummy cells with $Co(bpy)_3^{3+/2+}$ in acetonitrile as the electrolyte solution on TaON, RGO, RGO–TaON, and Pt CEs. The scan rate is 50 mV s^{-1}.

Table 1. Photovoltaic Performance and EIS Parameters of the DSSCs with Different CEs

CE	V_{oc} (mV)	J_{sc} (mA cm^{-2})	*FF*	η (%)	R_s (Ω cm^2)	R_{ct} (Ω cm^2)	Z_N (Ω cm^2)
Pt	835	13.73	0.69	7.91	1.7	1.8	2.7
RGO–TaON	829	13.38	0.69	7.65	2.1	1.9	3.0
RGO	814	12.33	0.46	4.62	1.9	6.9	7.4
TaON NPs	773	11.35	0.29	2.54	1.8	46.9	8.6

dx.doi.org/10.1021/am402353m | ACS Appl. Mater. Interfaces 2013, 5, 8217–8224

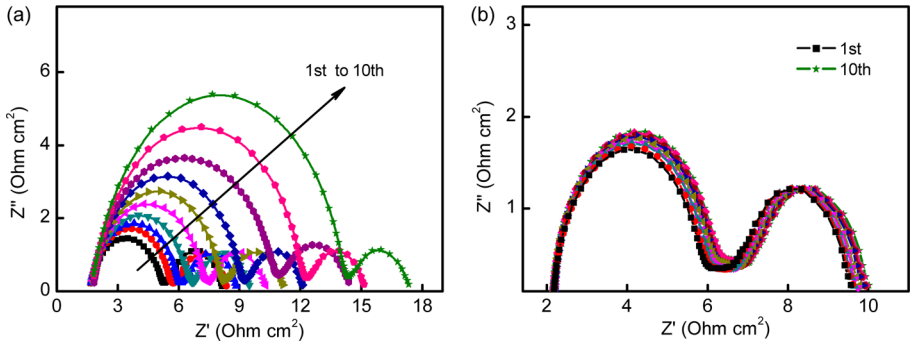

Figure 7. Nyquist plots of EIS for the potential cycling stability of the symmetric cells with Pt (a) and RGO−TaON (b) electrodes. The dummy cells were first subjected to cyclic voltammetry scanning of −1 to 1 V with a scan rate of 50 mV s^{-1} followed by a 20 s relaxation at 0 V, and then the EIS measurement at 0 V from 50 mHz to 1 MHz was performed. This sequence of electrochemical tests was repeated 10 times.

limiting current density (J_{lim}), which depends on the electron transfer rate at the CE−electrolyte interface for a redox electrolyte with a fixed concentration. A higher J_{lim} value signifies a higher catalytic activity of the CE. Figure 6a shows that the J_{lim} value increases in the order of TaON < RGO < RGO−TaON < Pt, but the J_{lim} value of RGO−TaON is approximately equal to that of Pt, suggesting that the RGO−TaON nanocomposite would have a similar electrocatalytic activity to that of the Pt CE. By contrast, the reduction reaction of $Co(bpy)_3^{3+}$ on the TaON or RGO is much slower. The result indicates that the incorporation of TaON NPs in the RGO network can lead to an enhancement of $Co(bpy)_3^{3+}$ reduction kinetics at the interface of the RGO−TaON CE.

Furthermore, Tafel polarization curves were also carried out on the symmetrical cells with TaON, RGO, RGO−TaON, and Pt CEs. In Figure 6b, the slope of the anodic or cathodic branch implies the exchange current density (J_0) on the electrode. The J_0 value of the RGO−TaON electrode, which is much larger than that of TaON and RGO, indicates its similar electrocatalytic function compared to the Pt electrode. Because a corresponding relationship exists between J_0 and R_{ct}, which is expressed as

$$J_0 = (RT)/(nFR_{ct})$$

where R is the gas constant, T is the absolute temperature, F is Faraday's constant, n is the stoichiometric number of electrons involved in the electrochemical reduction of $Co(bpy)_3^{3+}$, and R_{ct} is the charge-transfer resistance, J_0 can be calculated using the R_{ct} value from EIS spectra. The sequence of the calculated J_0 value (Pt ≈ RGO−TaON > RGO > TaON) is consistent with that derived from the Tafel polarization curves. Moreover, the Tafel polarization curves also shows the J_{lim} value, which determines Z_N as[53]

$$Z_N = \frac{kT}{ne_0S\sqrt{\frac{i\omega ne_0cl}{N_A}}J_{lim}} \tanh\left(\frac{2i\omega ne_0cN_A}{lJ_{lim}}\delta\right)$$

where e_0 is the elementary charge, c is the concentration of $Co(bpy)_3^{3+}$ species, l is the spacer thickness, N_A is the Avogadro constant, k is the Boltzmann constant, S is the electrode area, ω is the angular frequency, and δ is the thickness of the diffusion layer. It is found that the order of Z_N calculated from J_{lim} obtained in the Tafel polarization curves is fairly consistent with that from the EIS analysis (Table 1). Consequently, from the EIS and electrochemical analysis it can be concluded that the RGO−TaON nanocomposite has a much higher electrocatalytic activity than RGO or TaON and is comparable to that of the Pt electrode.

The electrochemical stability of the RGO−TaON and Pt CEs were examined using dummy cells by a sequential scan of CV and EIS for 10 cycles. As seen in Figure 7, R_s and Z_N can be basically considered to be maintained invariable after 10 CV−EIS cycling tests, which is similar to the earlier data reported on the cycling stability of Pt and graphene.[54] This indicates that the potential cycling does not affect the series ohmic resistance and the mass transport in the redox electrolyte. However, R_{ct} increases from 1.8 to 12.5 Ω cm^2 for Pt and from 1.9 to 2.1 Ω cm^2 for RGO−TaON. This result reveals that the RGO−TaON nanocomposite has a better electrochemical stability than the Pt electrode.

For counter electrodes in DSSCs, a high electrocatalytic activity of the CE materials plays a key role in improving the photovoltaic performance. On the basis of the above analysis, the use of the RGO−TaON nanocomposite as a CE can obviously reduce the charge-transfer resistance, showing a comparable electrocatalytic activity and better electrochemical stability to Pt CE. Therefore, the RGO−TaON nanocomposite is expected to be a promising alternative to the conventional Pt electrode in $Co(bpy)_3^{3+/2+}$-mediated organic DSSCs.

3.3. Photovoltaic Performance. Figure 8a shows the photocurrent density−voltage (J−V) characteristic curves of DSSCs using TaON, RGO, RGO−TaON, and Pt as CEs. The detailed photovoltaic parameters from the J−V curves are summarized in Table 1. Under 1 sun illumination, the TaON-based DSSC produces a short-circuit current density (J_{sc}) of 11.35 mA cm^{-2}, an open-circuit voltage (V_{oc}) of 773 mV, and a fill factor (FF) of 0.29, corresponding to a power conversion efficiency (η) of 2.54%, whereas the RGO-based DSSC produces a J_{sc} value of 12.33 mA cm^{-2}, a V_{oc} value of 814 mV, and an FF value of 0.46, corresponding to an η of 4.62%. As compared to TaON, the RGO CE produces a higher efficiency attributed to its much higher FF and slightly higher J_{sc} and V_{oc} values. The higher FF value for RGO is the result of its higher electrocatalytic activity, which facilitates the electron transfer from CE to the electrolyte and thus accounts for the higher J_{sc} value. The higher V_{oc} value for RGO is the result of its higher J_{sc} value.

For the DSSC with the RGO−TaON CE fabricated using exactly the same method, the values of J_{sc}, V_{oc}, and FF are 13.38 mA cm^{-2}, 829 mV, and 0.69, corresponding to an η of 7.65%. As compared to RGO or TaON alone, the much improved solar-cell performance for the RGO−TaON composite is attributed to the much improved electrocatalytic activity caused

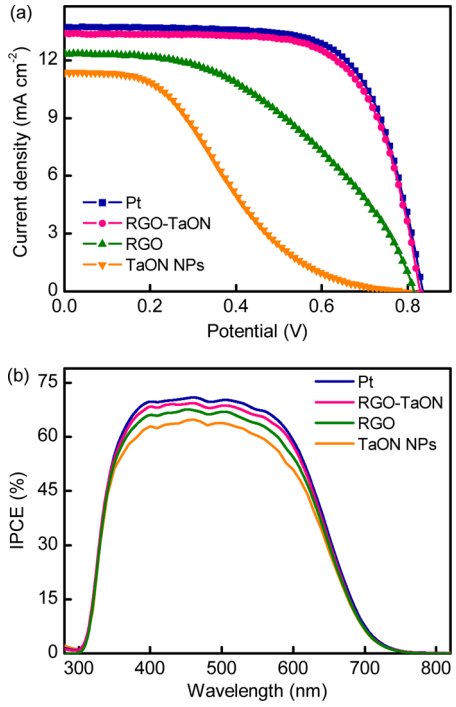

Figure 8. (a) Comparison of the *J*–V characteristics of DSSCs fabricated with TaON, RGO, RGO–TaON, and Pt CEs under 1 sun illumination (AM1.5G, 100 mW cm^{-2}). (b) IPCE spectra of the cells used in panel a.

by the synergistic effect (Figure 5). The significant enhancement of *FF* can be explained by the significant decrease in R_{ct} (Figure 5). The increase in J_{sc} is attributed to the fact that the high specific surface area of CE increases the total current of the Co(bpy)$_3^{3+/2+}$ redox reaction.[55,56] The improved V_{oc} for the RGO–TaON CE relative to that of TaON or RGO CEs is the result of increased J_{sc}. For comparison, DSSCs using RGT as the counter electrode are fabricated. Figure S7 shows the corresponding *J*–V curves, with the photovoltaic parameters summarized in Table S1. A simple blending of RGO and TaON produces a slightly better performance than RGO, and the photovoltaic performance seems to be attributed to the arithmetic summation of the catalytic performance from RGO and TaON (Figure 5). Evidently, no synergistic effect was observed for the simple blending because of the absence of intimate interactions between RGO and TaON as revealed by the Raman spectra (Figure S4). However, a distinct synergistic effect exists in the RGO–TaON nanocomposite owing to the intimate interactions between RGO and TaON as shown in the Raman spectra (Figure 3). As compared to the RGO–TaON composite, the much lower *FF* and η values for RGT highlight how important the direct loading of TaON NPs on GO nanosheets followed by in situ reduction of GO to RGO is.

As shown in Table 1, the efficiency for the RGO–TaON-based DSSC is comparable to that of the Pt-based DSSC under the same conditions, indicating that the RGO–TaON composite is a promising alternative to Pt as the CE in Co(bpy)$_3^{3+/2+}$-mediated DSSCs. The corresponding IPCE spectra in Figure 8b shows that the changing order of the IPCE in the range of 350–650 nm is consistent with the J_{sc} trend in Figure 8a.

In addition, TaON, RGO, RGO–TaON, and Pt CEs are also used in DSSCs with N719 dye as the sensitizer and I^-/I_3^- redox couple in acetonitrile as the electrolyte. The *J*–V curves and their photovoltaic parameters are shown in Figure S8 and Table S2, respectively. Obviously, the RGO–TaON nanocomposite is not appropriate for the reduction of I_3^- owing to its low electrocatalytic activity on the reduction of I_3^-.

4. CONCLUSIONS

The RGO–TaON nanocomposite with TaON NPs loaded on the surface or between the RGO sheets is successfully fabricated and applied as a new type of counter electrode material for DSSCs by a drop-casting method. For Co(bpy)$_3^{3+/2+}$-mediated DSSCs, the RGO–TaON nanocomposite exhibits a much higher electrocatalytic activity than each individual component because of the synergistic effect caused by the intimate interactions between them, resulting in a significantly improved fill factor and power conversion efficiency. The RGO–TaON nanocomposite exhibits comparable electrocatalytic activity to Pt, but the former is more stable than the latter when exposed to the Co(bpy)$_3^{3+/2+}$ electrolyte and subjected to potential cycling. Our discovery expands the architectures of RGO-based cathodes for high-performance Co(bpy)$_3^{3+/2+}$-mediated DSSCs.

■ ASSOCIATED CONTENT

Ⓢ Supporting Information

Synthesis and structures of FNE29 and Co(bpy)$_3^{3+/2+}$ redox couple; UV–vis absorption spectrum of FNE29; XRD pattern of GO; Raman spectra of RGO and RGT; EIS spectra of RGO–TaON with different weight ratios; conductivity measurement for RGO, TaON, and RGO–TaON; *J*–V characteristics of DSSC with RGT CE; *J*–V characteristics of N719-sensitized DSSCs with I^-/I_3^- in acetonitrile as electrolyte, and photovoltaic performance of the DSSCs. This material is available free of charge via the Internet at http://pubs.acs.org.

■ AUTHOR INFORMATION

Corresponding Author

*E-mail: zs.wang@fudan.edu.cn. Tel/Fax: (+86)21-5163-0345.

Present Address

[†]Key Laboratory of Atomic and Molecular Physics & Functional Materials of Gansu Province, College of Physics and Electronic Engineering, Northwest Normal University, 967 Anning East Road, Lanzhou 730070, P. R. China.

Notes

The authors declare no competing financial interest.

■ ACKNOWLEDGMENTS

The work was financially supported by the National Basic Research Program of China (no. 2011CB933302), the National Natural Science Foundation of China (90922004 and 51273045), STCSM (12JC1401500), the Shanghai Pujiang Program (11PJ1401700), the Jiangsu Major Program (BY2010147), and the Shanghai Leading Academic Discipline Project (B108).

■ REFERENCES

(1) O'Regan, B.; Grätzel, M. *Nature* **1991**, *353*, 737–740.

(2) Kim, S.; Lee, J. K.; Kang, S. O.; Ko, J.; Yum, J.-H.; Fantacci, S.; Angelis, F. D.; Censo, D. D.; Nazeeruddin, M. K.; Grätzel, M. *J. Am. Chem. Soc.* **2006**, *128*, 16701–16707.

(3) Gao, F.; Wang, Y.; Shi, D.; Zhang, J.; Wang, M.; Jing, X.; Baker, R. H.; Wang, P.; Zakeeruddin, S. M.; Grätzel, M. *J. Am. Chem. Soc.* **2008**, *130*, 10720–10728.

(4) Yum, J.-H.; Hagberg, D. P.; Moon, S.-J.; Karlsson, K. M.; Marinado, T.; Sun, L.; Hagfeldt, A.; Zakeeruddin, S. M.; Grätzel, M. *Angew. Chem., Int. Ed.* **2009**, *48*, 1576−1580.
(5) Wu, K.-L.; Li, C.-H.; Chi, Y.; Clifford, J. N.; Cabau, L.; Palomares, E.; Cheng, Y.-M.; Pan, H.-A.; Chou, P.-T. *J. Am. Chem. Soc.* **2012**, *134*, 7488−7496.
(6) Wang, M.; Chamberland, N.; Breau, L.; Moser, J.-E.; Baker, R.-H.; Marsan, B.; Zakeeruddin, S. M.; Grätzel, M. *Nat. Chem.* **2010**, *2*, 385−389.
(7) Tian, H. N.; Yu, Z.; Hagfeldt, A.; Kloo, L.; Sun, L. C. *J. Am. Chem. Soc.* **2011**, *133*, 9413−9422.
(8) Wang, H.; Zhang, X.; Gong, F.; Zhou, G.; Wang, Z.-S. *Adv. Mater.* **2012**, *24*, 121−124.
(9) Kim, D.; Ghicov, A.; Albu, S. P.; Schmuki, P. *J. Am. Chem. Soc.* **2008**, *130*, 16454−16455.
(10) Huang, F.; Chen, D.; Zhang, X. L.; Caruso, R. A.; Cheng, Y. B. *Adv. Funct. Mater.* **2010**, *20*, 1301−1305.
(11) Jang, Y. H.; Xin, X.; Byun, M.; Jang, Y. J.; Lin, Z.; Kim, D. H. *Nano Lett.* **2012**, *12*, 479−485.
(12) Guo, W.; Xu, C.; Wang, X.; Wang, S.; Pan, C.; Lin, C.; Wang, Z. L. *J. Am. Chem. Soc.* **2012**, *134*, 4437−4441.
(13) Bisquert, J.; Zaban, A.; Greenshtein, M.; Mora-Seró, I. *J. Am. Chem. Soc.* **2004**, *126*, 13550−13559.
(14) Haque, S. A.; Palomares, E.; Cho, B. M.; Green, A. N. M.; Hirata, N.; Klug, D. R.; Durrant, J. R. *J. Am. Chem. Soc.* **2005**, *127*, 3456−3462.
(15) O'Regan, B. C.; Walley, K.; Juozapavicius, M.; Anderson, A.; Mater, F.; Ghaddar, T.; Zakeeruddin, S. M.; Klein, C.; Durrant, J. R. *J. Am. Chem. Soc.* **2009**, *131*, 3541−3548.
(16) Yella, A.; Lee, H.-W.; Tsao, H. N.; Yi, C.; Chandiran, A. K.; Nazeeruddin, M. K.; Diau, E. W.-G.; Yeh, C.-Y.; Zakeeruddin, S. M.; Grätzel, M. *Science* **2011**, *334*, 629−634.
(17) Calogero, G.; Calandra, P.; Irrera, A.; Sinopoli, A.; Citro, I.; Di Marco, G. *Energy Environ. Sci.* **2011**, *4*, 1838−1844.
(18) Wu, M.; Lin, X.; Wang, Y.; Wang, L.; Guo, W.; Qi, D.; Peng, X.; Hagfeldt, A.; Grätzel, M.; Ma, T. *J. Am. Chem. Soc.* **2012**, *134*, 3419−3428.
(19) Gong, F.; Wang, H.; Xu, X.; Zhou, G.; Wang, Z.-S. *J. Am. Chem. Soc.* **2012**, *134*, 10953−10958.
(20) Gong, F.; Xu, X.; Li, Z.; Zhou, G.; Wang, Z.-S. *Chem. Commun.* **2013**, *49*, 1437−1439.
(21) Ahmad, S.; Yum, J.-H.; Xi, Z. X.; Grätzel, M.; Butt, H.-J.; Nazeeruddin, M. K. *J. Mater. Chem.* **2010**, *20*, 1654−1658.
(22) Tai, Q.; Chen, B.; Guo, F.; Xu, S.; Hu, H.; Sebo, B.; Zhao, X.-Z. *ACS Nano* **2011**, *5*, 3795−3799.
(23) Wang, H.; Feng, Q.; Gong, F.; Li, Y.; Zhou, G.; Wang, Z.-S. *J. Mater. Chem. A* **2013**, *1*, 97−104.
(24) Xiao, Y.; Lin, J.-Y.; Tai, S.-Y.; Chou, S.-W.; Yue, G.; Wu, J. *J. Mater. Chem.* **2012**, *22*, 19919−19925.
(25) Wu, J.; Yue, G.; Xiao, Y.; Huang, M.; Lin, J.; Fan, L.; Lan, Z.; Lin, J.-Y. *ACS Appl. Mater. Interfaces* **2012**, *4*, 6530−6536.
(26) Ju, M. J.; Kim, J. C.; Choi, H.-J.; Choi, I. T.; Kim, S. G.; Lim, K.; Ko, J.; Lee, J.-J.; Jeon, I.-Y.; Baek, J.-B.; Kim, H. K. *ACS Nano* **2013**, *7*, 5243−5250.
(27) Liao, Y.; Pan, K.; Wang, L.; Pan, Q.; Zhou, W.; Miao, X.; Jiang, B.; Tian, C.; Tian, G.; Wang, G.; Fu, H. *ACS Appl. Mater. Interfaces* **2013**, *5*, 3663−3670.
(28) Chen, L.; Guo, C. X.; Zhang, Q.; Lei, Y.; Xie, J.; Ee, S.; Guai, G.; Song, Q.; Li, C. M. *ACS Appl. Mater. Interfaces* **2013**, *5*, 2047−2052.
(29) Liu, C.-J.; Tai, S.-Y.; Chou, S.-W.; Yu, Y.-C.; Chang, K.-D.; Wang, S.; Chien, F. S.-S.; Lin, J.-Y.; Lin, T.-W. *J. Mater. Chem.* **2012**, *22*, 21057−21064.
(30) Yen, M.-Y.; Teng, C.-C.; Hsiao, M.-C.; Liu, P.-I.; Chuang, W.-P.; Ma, C.-C. M.; Hsieh, C.-K.; Tsai, M.-C.; Tsai, C.-H. *J. Mater. Chem.* **2011**, *21*, 12880−12888.
(31) Levy, R. B.; Boudart, M. *Science* **1973**, *181*, 547−849.
(32) Hwu, H. H.; Chen, J. G. *Chem. Rev.* **2005**, *105*, 185−212.
(33) Ganesan, R.; Lee, J. S. *Angew. Chem., Int. Ed.* **2005**, *44*, 6557−6560.
(34) Tomchenko, A. A.; Emelianov, I. L.; Khatko, V. V. *Sens. Actuators, B* **1999**, *57*, 166−170.
(35) Liu, F.; Li, L.; Mo, F.; Chen, J.; Deng, S.; Xu, N. *Cryst. Growth Des.* **2010**, *10*, 5193−5199.
(36) Jang, J.; Ham, D.; Ramasamy, E.; Lee, J.; Lee, J. S. *Chem. Commun.* **2010**, *46*, 8600−8602.
(37) Wu, M. X.; Lin, X.; Hagfeldt, A.; Ma, T. L. *Angew. Chem., Int. Ed.* **2011**, *50*, 3520−3524.
(38) Wu, M. X.; Lin, X.; Hagfeldt, A.; Ma, T. L. *Chem. Commun.* **2011**, *47*, 4535−4537.
(39) Gao, Q.; Wang, S.; Ma, Y.; Tang, Y.; Giordano, C.; Antonietti, M. *Angew. Chem., Int. Ed.* **2011**, *50*, 1−5.
(40) Kovtyukhova, N. I.; Ollivier, P. J.; Martin, B. R.; Mallouk, T. E.; Chizhik, S. A.; Buzaneva, E. V.; Gorchinskiy, A. D. *Chem. Mater.* **1999**, *11*, 771−778.
(41) Li, D.; Müller, M. B.; Gilje, S.; Kaner, R. B.; Wallace, G. G. *Nat. Nanotechnol.* **2008**, *3*, 101−105.
(42) Jeong, H. K.; Lee, Y. P.; Lahaye, R. J.; Park, M. H.; An, K. H.; Kim, I. J.; Yang, C. M.; Park, C. Y.; Ruoff, R. S.; Lee, Y. H. *J. Am. Chem. Soc.* **2008**, *130*, 1362−1366.
(43) Zussman, E.; Chen, X.; Ding, W.; Calabri, L.; Dikin, D. A.; Quintana, J. P.; Ruoff, R. S. *Carbon* **2005**, *43*, 2175−2185.
(44) Cai, D.; Song, M. *J. Mater. Chem.* **2007**, *17*, 3678−3680.
(45) Wang, H. L.; Liang, Y. Y.; Li, Y. G.; Dai, H. J. *Angew. Chem., Int. Ed.* **2011**, *50*, 10969−10972.
(46) Chen, W.; Yan, L.; Bangal, P. R. *J. Phys. Chem. C* **2010**, *114*, 19885−20292.
(47) Ferrari, A. C.; Robertson. *Phys. Rev. [Sect.] B* **2000**, *61*, 14095−14107.
(48) Englert, J. M.; Dotzer, C.; Yang, G.; Schmid, M.; Papp, C.; Gottfried, J. M.; Steinrück, H.-P.; Spiecker, E.; Hauke, F.; Hirsch, A. *Nat. Chem.* **2011**, *3*, 279−286.
(49) Roy-Mayhew, J. D.; Bozym, D. J.; Punckt, C.; Aksay, I. A. *ACS Nano* **2010**, *4*, 6203−6211.
(50) Liang, Y.; Li, Y.; Wang, H.; Zhou, J.; Wang, J.; Regier, T.; Dai, H. *Nat. Mater.* **2011**, *10*, 780−786.
(51) Gong, F.; Li, Z.; Wang, H.; Wang, Z.-S. *J. Mater. Chem.* **2012**, *22*, 17321−17327.
(52) Li, Z.; Gong, F.; Zhou, G.; Wang, Z.-S. *J. Phys. Chem. C* **2013**, *117*, 6561−6566.
(53) Hanch, A.; Georg, A. *Electrochim. Acta* **2001**, *46*, 3457−3466.
(54) Kavan, L.; Yum, J.-H.; Grätzel, M. *Nano Lett.* **2011**, *11*, 5501−5506.
(55) Yoon, C. H.; Vittal, R.; Lee, J.; Chae, W. S.; Kim, K. *Electrochim. Acta.* **2008**, *53*, 2890−2896.
(56) Liu, C.-J.; Tai, S.-Y.; Chou, S.-W.; Yu, Y.-C.; Chang, K.-D.; Wang, S.; Chien, F. S.-S.; Lin, J.-Y.; Lin, T.-W. *J. Mater. Chem.* **2012**, *22*, 21057−21064.